

Manipulation of interlayer spacing and surface charge of carbon nanosheets for robust lithium/sodium storage



Cai Gao, Jianze Feng, Jingrou Dai, Yuanyuan Pan, Yulong Zhu, Wenhong Wang, Yunfa Dong, Linfang Cao, Lu Guan, Lei Pan, Han Hu*, Mingbo Wu*

State Key Laboratory of Heavy Oil Processing, Institute of New Energy, College of Chemical Engineering, China University of Petroleum (East China), Qingdao, 266580, China

ARTICLE INFO

Article history:

Received 8 May 2019

Received in revised form

22 June 2019

Accepted 13 July 2019

Available online 14 July 2019

ABSTRACT

The sluggish kinetics in anode materials severely prevents the practical use of lithium/sodium-ion batteries in many current and emerging applications. To overcome this bottleneck, we report a facile and scalable strategy to construct nitrogen and phosphorus co-doped carbon nanosheets with abundant electron-rich regions rendering a strong cation attraction and expanded interlayer spacing for fast lithium/sodium diffusion, which allows excellent rate capable anodes for lithium/sodium-ion batteries. Specifically, the as-prepared nanosheets afford outstanding pseudocapacitive behavior with superior rate capacities of 379 and 140 mA h g⁻¹ at a high current density of 5.0 A g⁻¹ for lithium and sodium storage, respectively, while the calendar life can be as long as thousands of cycles. The extraordinary rate capability is further demonstrated through combined use of quantitative kinetics analysis, galvanostatic intermittent titration technique measurements and theoretical simulation. Considering the extraordinary electrochemical performance and comprehensive analysis of pseudocapacitive lithium/sodium storage mechanism, this work holds great potential to serve as a fundamental reference for exploring robust pseudocapacitive electrode materials.

© 2019 Elsevier Ltd. All rights reserved.

1. Introduction

With the imminent shortage of fossil fuel and increasing concern on environment pollution, the innovation of electrical energy storage systems is becoming crucial and urgent [1–5]. In this regard, focused attention has been paid to lithium-ion batteries (LIBs) and/or sodium-ion batteries (SIBs) because of their appealing features and great promise for many sustainable applications [6–13]. Despite the feasibility of delivering high energy density by these devices, their low power density largely restricts their possibility to satisfy more and more applications with high power demand [14]. Thus, tremendous research efforts have been devoted to simultaneously rendering these devices with high energy density and power capability [15,16]. One critical limitation comes from the anode materials generally operated using diffusion-controlled mechanism, which always delivers sluggish reaction dynamics. More specifically, the insertion of lithium and sodium ions into

bulk-phase graphite and hard carbon anodes, respectively, essentially slows down at high rates [17]. As such, it is imperative to accelerate the solid-state diffusion of lithium/sodium in the electrode materials.

The employment of pseudocapacitive charge storage has been considered as one of the most viable and promising technologies to surmount the sluggish ion diffusion in electrode materials and accomplish high-rate capability for these devices [18–21]. Normally, the pseudocapacitive charge storage is a surface-driven capacitive process, different from the diffusion-controlled intercalation process for traditional battery electrodes [22–26]. Therefore, one key rationale is to manipulate the bulk-size anode materials into low-dimensional nanostructured materials [27–31]. In this spirit, Zhao and his colleagues reported the controllable synthesis of two-dimensional carbon nanosheets for efficient lithium storage, especially at high rates [32]. In addition, expanding interlayer spacing has also been demonstrated as a promising strategy to enhance the rate capability of nanostructured electrode for lithium/sodium storage. For example, Wang et al. expanded the interlayer spacing of graphite from 0.34 to 0.43 nm and realized robust reversible sodium storage where the discharge/charge curves are

* Corresponding authors.

E-mail addresses: hhu@upc.edu.cn (H. Hu), wumb@upc.edu.cn (M. Wu).

almost plateau-free [33]. Very recently, another appealing method based on construction of electron-rich regions on electrode surfaces has also offered promising potential as these regions can contribute to a strong attraction to cations, thus boosting the rate performance [22,34,35]. Based on the aforementioned design rationales, two-dimensional carbon nanosheets with electron-rich surface and expanded interlayer spacing are expected to deliver outstanding pseudocapacitive lithium/sodium storage because of the synergistic effects arising from these rationally combined structural merits. However, the designed construction of such a nanostructured anode material, especially in a simple and cost-effective manner, remains a great challenge.

In the present work, we report the incorporation of abundant electron-rich regions into the carbon nanosheets and expansion of their interlayer spacing through high content of nitrogen and phosphorus co-doping. These nitrogen and phosphorus co-doped carbon nanosheets (NP-CNSs) are facilely synthesized by carbonizing petroleum asphalt in the presence of melamine and supermolecular polymer made of phytic acid and melamine, where the nitrogen and phosphorus content is as high as 11.2 and 5.8 at. %, respectively. The NP-CNSs thus afford a large specific capacity, superior cyclability, especially excellent rate performance for lithium/sodium storage. Intrigued by the extraordinary rate capability, quantitative kinetics analysis has been applied to explore the detailed surface-driven contribution, which is as high as 65.5% and 76.1% for lithium and sodium storage, respectively, at a scan rate of 1.2 mV s^{-1} . Then, this enhancement has been explicitly explained using galvanostatic intermittent titration technique (GITT). Moreover, the electron-rich regions have been confirmed through the theoretical calculation.

2. Experimental

2.1. Synthesis of the NP-CNSs

Petroleum asphalt was provided by Sinopec Group. At room temperature, 5 mL of phytic acid (70%, Aladdin) and 1.2 g of melamine (99%, Aladdin) were assembled into a supermolecular polymer in water. The supermolecular polymer was collected by centrifugation and freeze-drying overnight. Then, 1.5 g of petroleum asphalt, 0.8 g of melamine and 0.7 g of the supermolecular polymer were thoroughly mixed in a mortar. The obtained powder was calcined at 800°C for 2 h with the heating rate of $5^\circ\text{C}/\text{min}$ under a continuous nitrogen flow. The N, P co-doped carbon nanosheets (NP-CNSs) were collected without further washing and cleaning after the furnace cooling down to room temperature.

2.2. Synthesis of the N-CNSs

The synthesis of the N-doped carbon nanosheets (N-CNSs) is similar to the synthesis of NP-CNSs except the absence of supermolecular polymer.

2.3. Synthesis of the NP-PAC

The synthesis of the N, P co-doped petroleum asphalt carbon (NP-PAC) is similar to the synthesis of NP-CNSs except the absence of melamine.

2.4. Synthesis of the PAC

Bare petroleum asphalt was calcined at 800°C for 2 h with a heating rate of $5^\circ\text{C}/\text{min}$ in N_2 to obtain petroleum asphalt carbon (PAC).

2.5. Materials characterization

Scanning electron microscopy (SEM) observation was performed on Hitachi S-4800 and transmission electron microscopy (TEM) images were obtained on JEM-2010 system at an accelerating voltage of 200 kV. Energy dispersive spectroscopy (EDS) was collected on an EDAX system attached on the TEM system. X-ray diffraction (XRD) with Cu $K\alpha$ radiation ($\lambda = 1.5406 \text{ \AA}$) was carried out on an X'Pert PRO MPD diffractometer. Raman spectra were detected on Renishaw RM2000 (512 nm laser). The Brunner–Emmet–Teller (BET) specific surface area was measured by a Micromeritics ASAP 2020 analyzer. The surface elemental compositions were detected using an X-ray photoelectron spectroscopy (XPS, Thermo Scientific Escalab 250XI) with Al $K\alpha$ radiation. The zeta potential was tested by Nano ZS Zeta Light Scattering Instrument, Malvern Instruments Co., Ltd.

2.6. Electrochemical measurements

The homogeneous slurry was prepared by mixing the active material, carbon black, and polyvinylidene difluoride with a weight ratio of 8:1:1, then coated on a copper current collector, and transferred to a vacuum oven at 80°C for 12 h. The loading mass of active species was $0.7\text{--}0.9 \text{ mg cm}^{-2}$. CR2032 coin-type half cells were assembled with Li/Na metals as the counter electrode and reference electrode and employed the 1 M LiPF_6 and 1 M NaClO_4 in dimethyl carbonate and ethylene carbonate (1:1 vol%) as the electrolyte. The charge-discharge curves, cyclic voltammetry (CV) curves, and electrochemical impedance spectroscopy (EIS) were obtained on the Land Battery Measurement System at a potential window of 0.01–3 V, CHI760D electrochemical workstation, Autolab PGSTAT204, respectively. The Li^+/Na^+ diffusivity of the NP-CNSs electrode was measured by the galvanostatic intermittent titration technique (GITT) via which the cell was evaluated at a pulse current of 50 mA g^{-1} for 40 min at 2 h rest intervals.

2.7. DFT calculations

Density functional theory (DFT) calculations were implemented by Vienna Ab Initio Simulation Package (VASP). We built 10×10 supercell of graphene with nitrogen, oxide and phosphorus functional groups to mimic the observed graphene at nanoscale as shown in Fig. 3e, Fig. 3f and Fig. S7. Ion-electron interactions were described by projected augmented wave (PAW)-pseudopotential. Exchange and correlation interactions were calculated with generalized gradient approximation (GGA) of Perdew–Burke–Ernzerhof (PBE) form. The geometry optimizations and electronic calculations were performed with the cutoff energy of 500 eV and the convergence threshold for residual force of 0.01 eV \AA^{-1} . Brillouin zone integration was carried out at $2 \times 2 \times 1$ Monkhorst-Pack mesh of k points. The vacuum spacing is at least 15 \AA to avoid the interaction between the two slabs of graphene. The analysis of charge distributions was used by the Bader's scheme.

3. Results and discussion

The synthesis procedure of NP-CNSs is illustrated in Fig. 1. For the purpose of cost-effective synthesis, cheap raw materials such as petroleum asphalt, melamine, and phytic acid were employed in our research. The melamine and phytic acid constructed supermolecular polymer [36], melamine, and petroleum asphalt were firstly mixed and then annealed in nitrogen atmosphere at 800°C for 2 h, via which the NP-CNSs were efficiently produced. The melamine would first be condensed into graphitic carbon with

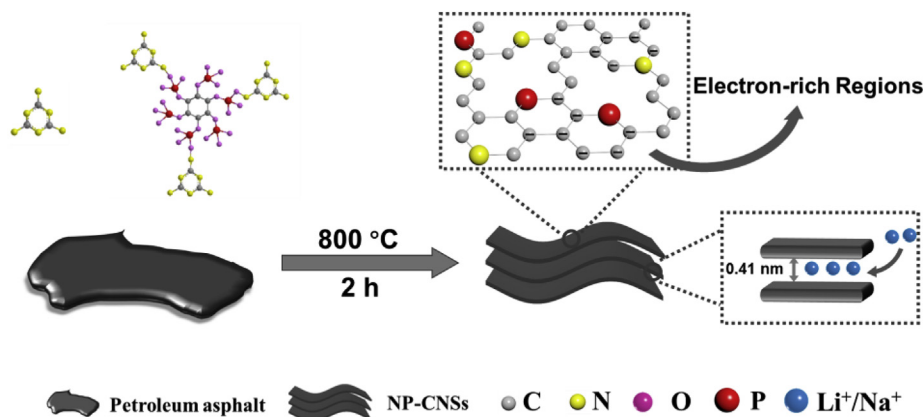


Fig. 1. Schematic illustration of synthesizing NP-CNSs. (A colour version of this figure can be viewed online.)

two-dimensional nanosheets at elevated temperatures and then decompose, which holds great potential to serve as sacrificed templates [37]. The petroleum asphalt, melted at elevated temperatures [38,39], would be guided to carbonize into two-dimensional carbon nanosheets. Meanwhile, melamine can also serve as the nitrogen source while the supermolecular polymer contributes to phosphorus doping and additional nitrogen doping.

To highlight the melamine-derived template direct-synthesis, bare petroleum asphalt, the mixture of petroleum asphalt and melamine as well as the mixture of petroleum asphalt and supermolecular polymer were also annealed under the same condition. Without melamine, petroleum asphalt-derived carbon (PAC) and N, P co-doped petroleum asphalt-derived carbon (NP-PAC) exist as irregular bulk particles, as shown in Fig. S1 and Fig. S2. The sole introduction of melamine could contribute to a nitrogen-doped carbon with two-dimensional morphology (denoted as N-CNSs) as revealed in Fig. S3. The nanosheet morphology of the NP-CNSs has been confirmed by scanning electron microscopy (SEM) observation in Fig. 2a and b. The formation of the nanosheet morphology in the presence of melamine demonstrates its

essential role as in this morphology controlled synthesis.

Then, the microscopic details were further revealed using transmission electron microscopy (TEM). The N-CNSs (Fig. S3b) and NP-CNSs (Fig. 2c) are almost transparent to the electron beam, indicative of their thin thickness. Moreover, the interlayer spacing for PAC, NP-PAC, N-CNSs, and NP-CNSs, observed under high-resolution TEM (HRTEM), is 0.34 nm (Fig. S1c), 0.41 nm (Fig. S2c), 0.37 nm (Fig. S3c), and 0.41 nm (Fig. 2d), respectively. The enlargement of spacing is mainly due to the larger covalent radius of N and P atoms [40], which holds great possibility to reduce the diffusion barrier of lithium/sodium ions. The specific surface area and pore size distribution of these three samples were analyzed using nitrogen sorption method. As shown in Fig. S4, NP-CNSs ($111.82 \text{ m}^2 \text{ g}^{-1}$) are obviously superior to N-CNSs ($34.21 \text{ m}^2 \text{ g}^{-1}$), NP-PAC ($10.65 \text{ m}^2 \text{ g}^{-1}$) and PAC ($3.25 \text{ m}^2 \text{ g}^{-1}$) in term of specific surface area and porosity, which will provide higher contact area and facilitated diffusion path for electrolyte [18].

The structure, composition and chemical states of these carbon materials were thoroughly analyzed by X-ray diffraction (XRD), Raman, X-ray photoelectron spectroscopy (XPS). The XRD patterns

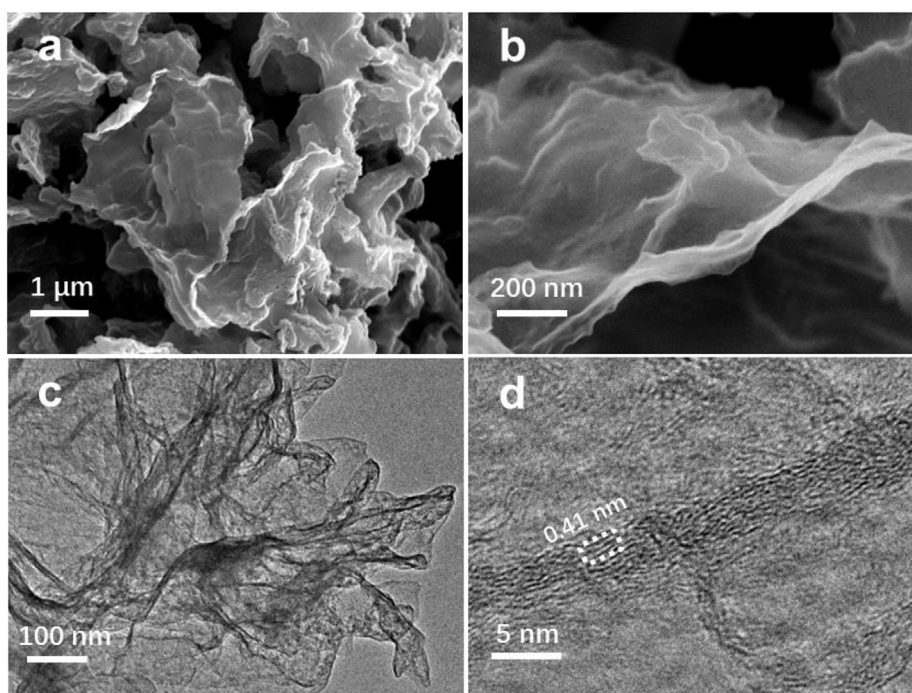


Fig. 2. (a) and (b) SEM images, (c) TEM image and (d) HRTEM image of NP-CNSs.

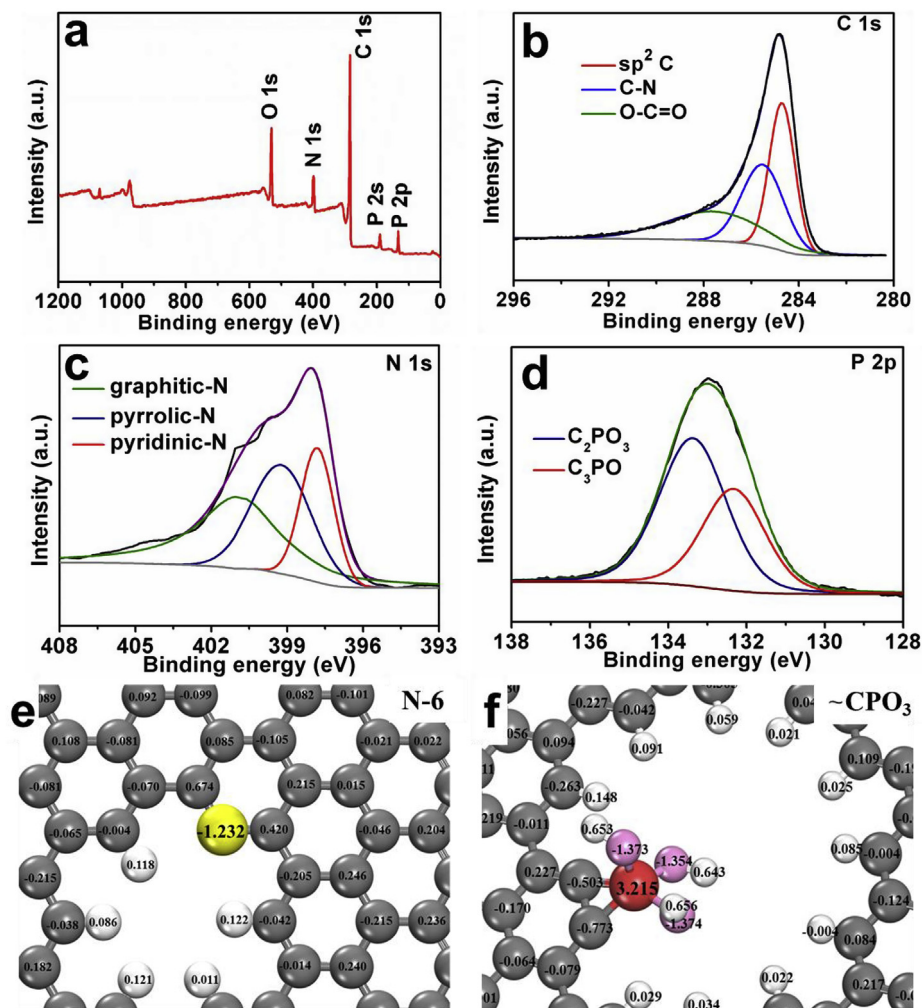


Fig. 3. (a) XPS spectra of the NP-CNSs. XPS high-resolution spectra of (b) C 1s and (c) N 1s, and (d) P 2p for the NP-CNSs. (e and f) The charge distributions of functional groups containing N and P by DFT calculations. (Grey ball: carbon atom; white ball: hydrogen atom; yellow ball: nitrogen atom; red ball: phosphorus atom; pink ball: oxygen atom.). (A colour version of this figure can be viewed online.)

in Fig. S5a reveal the typical feature of amorphous structure and the detailed structural parameters based on these profiles are listed in Table S1. The gradually increased interlayer spacing from PAC to N-CNSs and NP-PAC and NP-CNSs is reflected from the low angle shift of (002) diffraction peak, which is in good agreement with HRTEM observation. The domain thickness and width, as reflected from Table S1, show very limited variation. Fig. S5b shows the Raman spectra of PAC, NP-PAC, N-CNSs, and NP-CNSs. All of them exhibit two remarkable peaks around 1355 and 1586 cm^{-1} , related to the D-band and G-band of carbon. Besides, NP-CNSs and NP-PAC showcase the highest I_D/I_G ratio because of heavier structural distortion caused by dual doping [41]. The XPS surveys show that N content in N-CNSs is around 8.9 at. % (Fig. S6) while the N content is as high as 11.2 at. % for NP-CNSs (Fig. 3a), revealing the additional doped N provided by the supermolecular polymer. The N and P content in NP-PAC are around 10.1 at. % and 5.43 at. % (Fig. S6d). Meanwhile, the P content in NP-CNSs is also quite high, reaching to 5.8 at. % (Fig. 3a). The high-resolution C 1s spectrum (Fig. 3b) can be deconvoluted into three peaks, namely, the main peak at 284.2 eV associated with sp^2 C, the peak at 285.2 eV related to C–N and a minor peak at 288.1 eV describing O–C=O bond. The N 1s spectrum (Fig. 3c) can also be disassembled into three peaks, which express the existence of pyridinic-N (397.8 eV), pyrrolic-N (399.7 eV) and graphitic-N (400.8 eV). Fig. 3d shows the P 2p spectrum and two

peaks fitted to P–C (132.3 eV) and P–O bond (133.4 eV) are observed. Recent investigations revealed that the heteroatoms in carbon frameworks can contribute to electron-rich regions for enhanced cation attraction, which is favorable for pseudocapacitive energy storage [22,34]. Thus, the influence of the related surface groups on charge distribution was analyzed through density functional theory (DFT) calculations. Herein, the charge redistribution induced by different functional groups of NP-CNSs was mainly studied. In Fig. 3e–f and Fig. S7, the charge changes of carbon atoms around a specific group such as pyridinic-N (N-6) and phosphate group ($\sim\text{C}_2\text{PO}_3$) are significant (e.g., from -0.011 to -0.773), but the influences of the graphite-N (N-Q) is relatively small (e.g., from -0.002 to -0.097). In Table S2, all the related samples offer a negative zeta potential where the value of NP-CNSs is obviously the smallest among all these samples, demonstrating the strongest potential for cation attraction [42]. Considering the high content of doped N and P, abundant electron-rich regions can thus be effective incorporated. Undoubtedly, these electron donors would afford a strong attraction to the electron acceptors, namely, lithium or sodium ions, which essentially leads to high rate capability [34].

To assess the lithium storage behavior, the NP-CNSs electrode was first tested by cyclic voltammetry (CV) in the voltage range of 0.01 and 3 V (vs. Li^+/Li). As shown in Fig. 4a, the CV curves of NP-CNSs exhibit typical feature of carbonaceous materials [43]. The

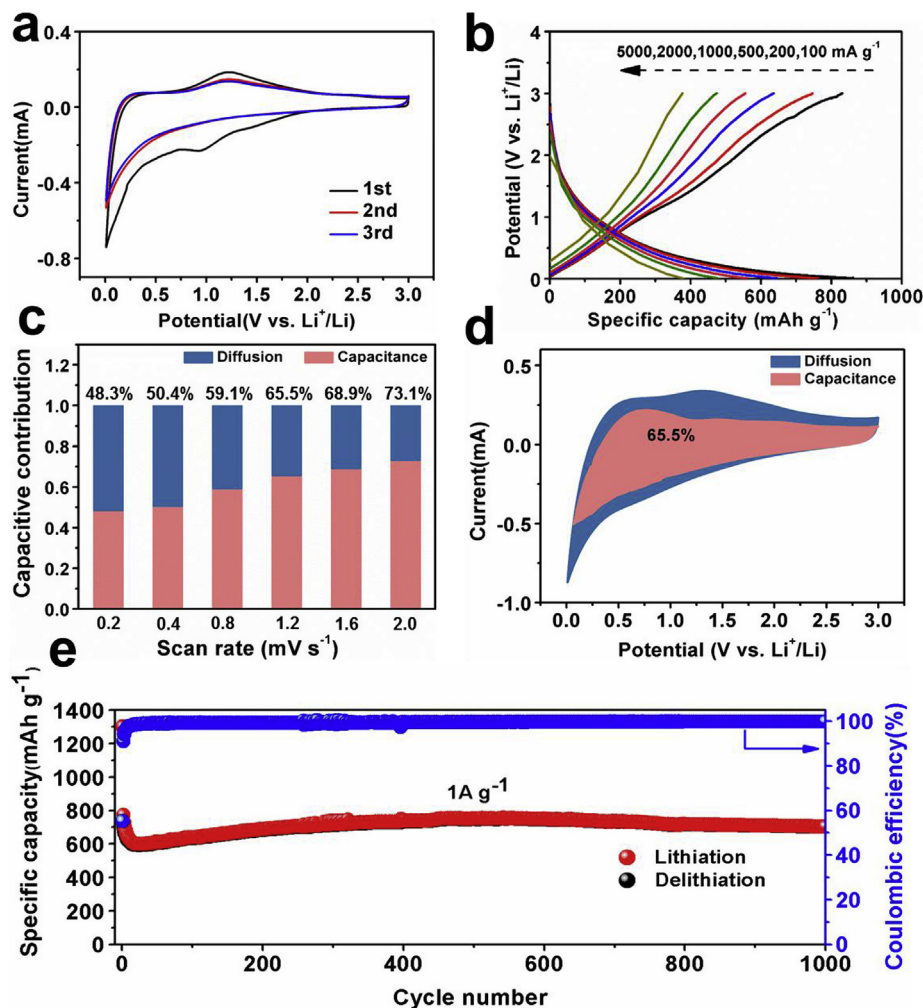


Fig. 4. (a) Cyclic voltammetry of the NP-CNSs at a rate of 0.2 mV s^{-1} . (b) Galvanostatic charge/discharge profiles of the NP-CNSs at various current densities. (c) The capacitive contributions of NP-CNSs at different scan rates. (d) Contribution of the capacitive current to the overall cyclic voltammetry response at 1.2 mV s^{-1} in LIBs. (e) Cycle performance of NP-CNSs at 1 A g^{-1} . (A colour version of this figure can be viewed online.)

broad peak between 1.5 and 0.25 V only appears in the first discharge cycle, which could be related to the formation of solid electrolyte interface (SEI) films [44]. The cathodic peak at 0.01 V and the anodic peak at 1.2 V are assigned to the reversible insertion/extraction of Li^+ in carbon nanosheets [45]. Besides, the subsequent CV curves are overlapped, revealing a high reversibility. Figs. S8a and b present the cyclic performance of NP-CNSs at a current density of 200 mA g^{-1} . The initial lithiation and delithiation capacities are 1532 mAh g^{-1} and 908.2 mAh g^{-1} , respectively, with an initial coulombic efficiency of 59.3%. After 100 discharge/charge cycles, a high reversible capacity of 760 mAh g^{-1} is afforded. The rate capability of the NP-CNSs at different current densities from 0.1 to 5 A g^{-1} is shown in Fig. S8c. An average capacity of 857, 762, 647, 560, 481, and 379 mAh g^{-1} is delivered at a current density of 100, 200, 500, 1000, 2000, and 5000 mA g^{-1} , respectively. Then, the capacity can be restored to 850 mAh g^{-1} when the current density was set to 100 mA g^{-1} again. Obviously, the rate performance of the NP-CNSs is far superior to that of N-CNSs, NP-PAC and PAC. All discharge/charge curves of NP-CNSs at different current densities (Fig. 4b) are almost plateau-free, revealing a high possibility of pseudocapacitive energy storage [46]. As a result, quantitative kinetics analysis of the lithium storage processes was conducted. The CV curves of the NP-CNSs at scan rates ranging from 0.2 to 2.0 mV s^{-1} were carried out, where the results are exhibited in

Fig. S8d. Generally, the current contribution at a particular potential consists of capacitive portion and diffusion-controlled portion, which are expressed as k_1v and $k_2v^{1/2}$, respectively. Their relationship can be described as follow:

$$i = av^b = k_1v + k_2v^{1/2} \quad (1)$$

In this relationship, a , k_1 and k_2 are constants, while v is the scan rate. The b value, which can be determined by calculating the slope of the $\log(v)$ - $\log(i)$ plots, ranges from 0.5 (diffusion-controlled contribution) to 1 (capacitive contribution) [47–49]. The detailed results were exhibited in Fig. S8e. As shown, a b value larger than 0.8 is observed at a wide range of potential, which reveals a dominated capacitive contribution for the NP-CNSs electrodes. Then, the k_1 and k_2 values were calculated for quantitatively determining the contribution of capacitive energy storage at different scan rates. As clearly revealed in Fig. 4c, the capacitive contribution increases with the increasing of the scan rates, which can be as high as 73.1% at a scan rate of 2 mV s^{-1} . Even at a moderate scan rate of 1.2 mV s^{-1} , the contribution from capacitance can be as high as 65.5% as shown in Fig. 4d, indicative of a robust pseudocapacitive lithium storage. Fig. 4e describes the long-term stability, which was determined through repeatedly discharging and charging for 1000 cycles at a current density of 1 A g^{-1} . After a mild

increase in capacity for the first few cycles, a high specific capacity of 706 mAh g^{-1} is delivered and remains almost unchanged in the following cycles. This capacity increase in LIBs may be due to the reversible formation of polymeric gel-like film by electrolyte degradation, which provides extra Li^+ storage capacity [50,51]. On the other hand, the reversible capacity of 453, 398 and 221 mAh g^{-1} is afforded by N-CNSs, NP-PAC and PAC electrodes (Fig. S8f), respectively, which is inferior to the NP-CNSs electrode. A comparison between the storage capability of NP-CNSs and carbon materials previously reported is shown for both LIBs (Table S3), indicating the excellent electrochemical performance of NP-CNSs.

Then sodium storage capacity of the NP-CNSs electrode was also evaluated through the similar procedure. As revealed from the CV curves in Fig. 5a, the first discharge gives two irreversible cathode peaks at 0.85 and 0.35 V corresponding to the inevitable formation of the SEI film [52]. Then, the high reversibility is reflected from the almost fully overlapped CV curves in the subsequent cycles. Fig. S9a shows the cyclic stability of NP-CNSs electrode at a current density of 200 mA g^{-1} . The charge capacity of 285 mAh g^{-1} is produced for the first cycles with an initial coulombic efficiency of 42.1%, and the capacity retention is as high as 82% after 100 cycles. Then the rate capacity was evaluated at various current densities ranging from

100 to 5000 mA g^{-1} . As shown in Fig. S9b, the reversible capacity of 268, 241, 214, 192, 171, and 140 mAh g^{-1} is afforded at a current density of 100, 200, 500, 1000, 2000, and 5000 mA g^{-1} , respectively, which is substantially superior to N-CNSs, NP-PAC and PAC under the same evaluated condition. The restoration of the current density back to 100 mA g^{-1} can lead to the increase of specific capacity from 140 to around 230 mAh g^{-1} , indicative of the excellent reversible sodium storage. The sloping discharge-charge curves exhibited in Fig. 5b afford the typical feature of capacitive energy storage [46]. Thus, the quantitative kinetics analysis was conducted to reveal the exact capacitive contribution. Similar to that of lithium storage measurements, the peak current of the CV curves increases together with the increasing scan rates as shown in Fig. S9c. The careful calculation reveals that a series of b values larger than 0.8 are observed at all the tested potentials in Fig. S9d, which demonstrates the dominated pseudocapacitive sodium storage processes throughout the entire potential range. Then, the capacitive contributions at different scan rates were revealed in Fig. 5c. As shown, the increase of scan rates from 0.2 to 2.0 mV s^{-1} can lead to the augment of capacitive portion from 59.2% to 83.5%. Fig. 5d gives an intact description of the capacitive contribution at a scan rate of 1.2 mV s^{-1} for sodium storage, which is as high as 76.1%. The

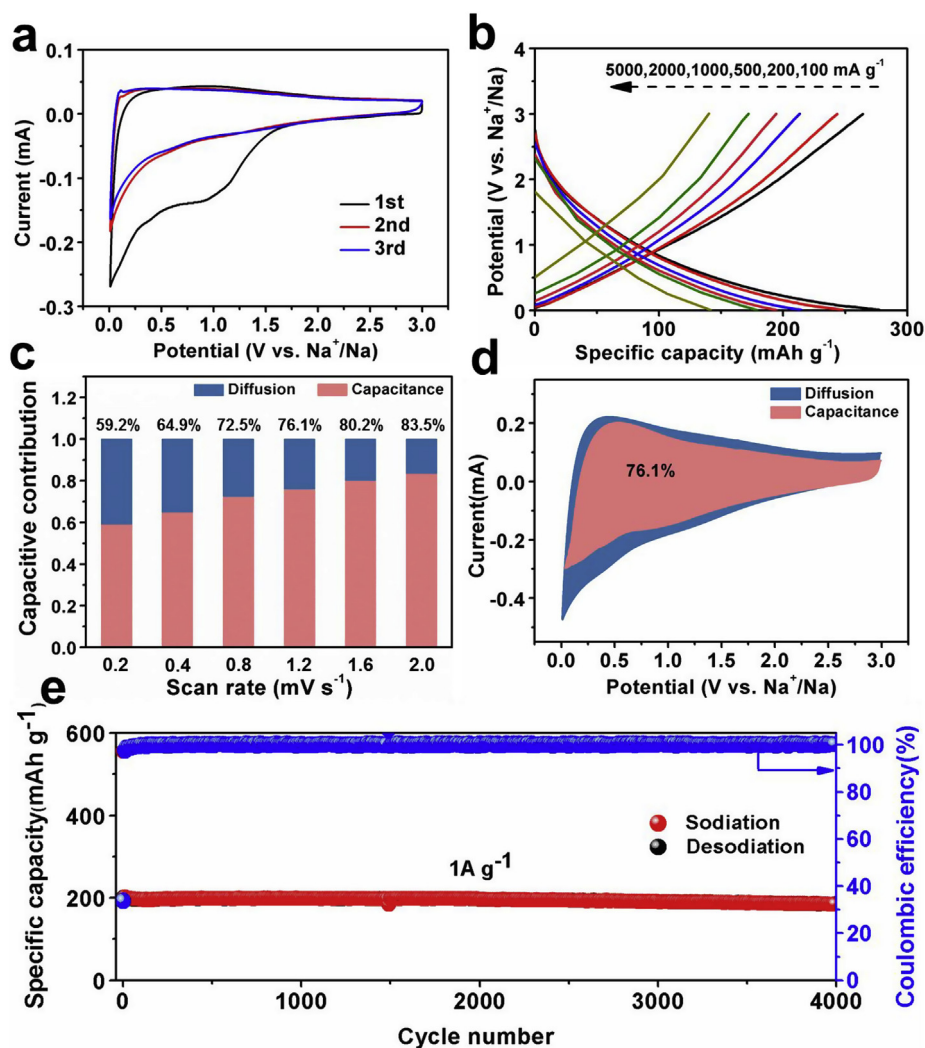


Fig. 5. (a) Cyclic voltammetry of the NP-CNSs at a rate of 0.2 mV s^{-1} . (b) Galvanostatic charge/discharge profiles of the NP-CNSs at various current densities. (c) The capacitive contributions of NP-CNSs at different scan rates. (d) Contribution of the capacitive current to the overall cyclic voltammetry response at 1.2 mV s^{-1} in SIBs. (e) Cycle performance of NP-CNSs at 1 A g^{-1} . (A colour version of this figure can be viewed online.)

cyclability of the NP-CNS is also appealing. As shown in Fig. 5e, a high specific capacity of 187 mAh g⁻¹ is afforded after 4000 cycles at 1000 mA g⁻¹, which accounts for a capacity retention of 94%. This excellent cyclability is superior to many previous results of carbonaceous anodes (Table S4).

To shed light on the extraordinary lithium/sodium capability, especially the rate performance, electrochemical impedance spectroscopy (EIS) and galvanostatic intermittent titration technique (GITT) measurement were conducted. In the high frequency ranges, the Nyquist plots of NP-CNSs in Fig. S10 give depressed semicircles for both lithium and sodium storage, suggesting the lower charge transfer resistance. In addition, the equivalent circuit has been fitted according to the spectra (Fig. S10). The similar circuits for lithium and sodium storage indicate the almost identical mechanism for these two cations [53]. To get an insightful understanding of Li⁺/Na⁺ diffusion dynamics, GITT was applied for the 2nd and 3rd cycles of lithium and sodium storage. In this technology, the diffusion coefficient (D) of Li⁺/Na⁺ can be expressed using the following equation [54]:

$$D = \frac{4}{\pi\tau} \left(\frac{m_B V_M}{M_B S} \right)^2 \left(\frac{\Delta E_S}{\Delta E_T} \right)^2 \quad (2)$$

where τ is the duration of current pulse, m_B the active mass of the electrode, M_B the molar mass, V_M the molar volume of the electrode, S the surface area of the NP-CNSs electrodes, and ΔE_S and ΔE_T

are the voltage change due to the current pulse and the voltage change during the current pulse, respectively. Fig. 6a and b shows the discharge/charge curves and corresponding diffusion coefficient of Li⁺/Na⁺ in GITT measurement for NP-CNSs electrode in the 2nd and 3rd cycles. During the whole cycles, the D value of Li⁺/Na⁺ varies in a small range and remains quite high, suggesting a very fast diffusion rate of Li⁺/Na⁺ in the framework of NP-CNSs. These results are in very good agreement with the aforementioned measurements. It suggests that the high content of nitrogen and phosphorous doping induced abundant electrode-rich region and expansion of interlayer spacing are responsible for the excellent performance.

4. Conclusion

In summary, a facile strategy employing lost-cost precursors such as petroleum asphalt, melamine, and phytic acid has been proposed to produce carbon nanosheets with high nitrogen and phosphorus doping. The incorporated nitrogen and phosphorus induce charge redistribution and distortion of the graphene layer, thus contributing to abundant electron-rich regions and expanded interlayer spacing, respectively. These structural merits not only generate a strong attraction to cations but also reduce the diffusion barrier for lithium/sodium in the carbon frameworks. The as-prepared nitrogen and phosphorous co-doped carbon nanosheets (NP-CNSs) thus deliver outstanding lithium and sodium storage

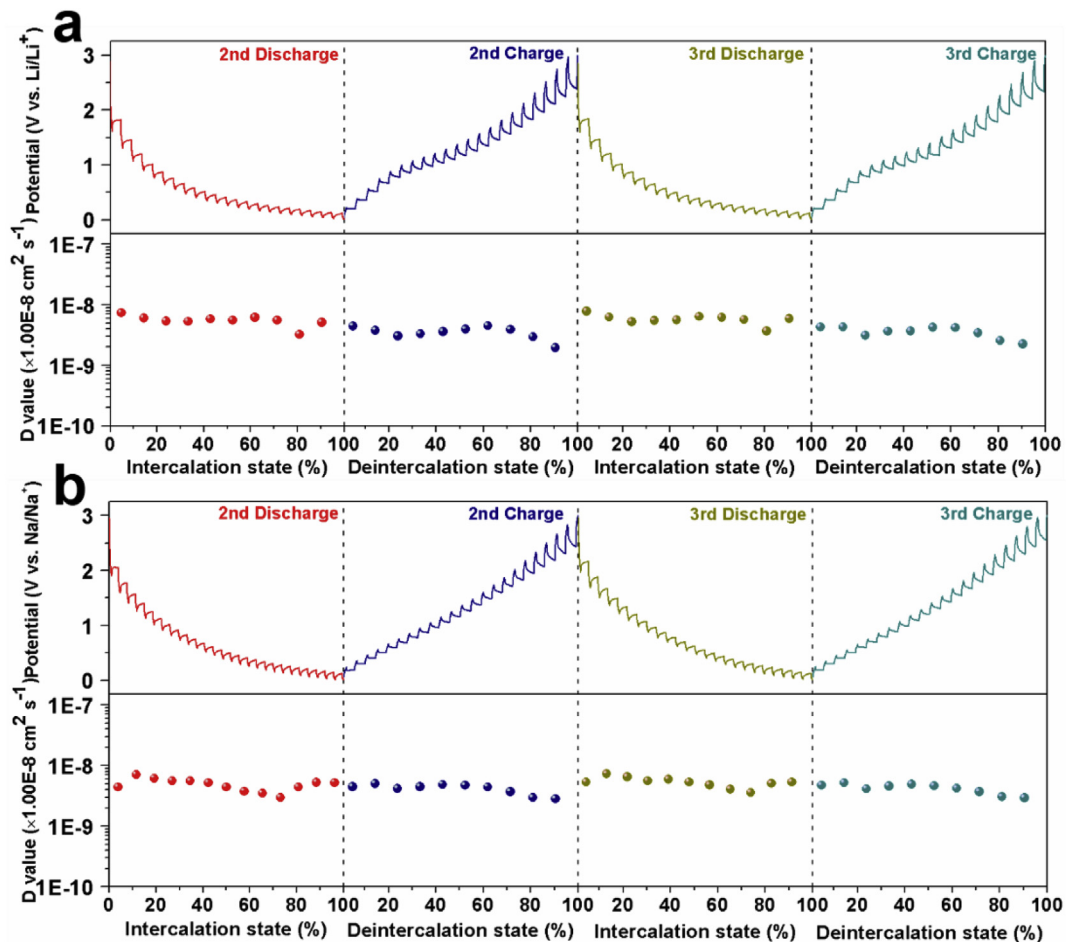


Fig. 6. The discharge/charge curves in GITT measurement and the corresponding diffusivity coefficient (D) in the discharge and charge processes of NP-CNSs in the 2nd and 3rd cycles in (a) LIBs and (b) SIBs. (A colour version of this figure can be viewed online.)

capabilities with large specific capacity, high rate capability, and outstanding cyclic performance. An insightful understanding of the outstanding performance was put forward through comprehensive analysis using quantitative kinetics analysis, galvanostatic intermittent titration technique measurements and theoretical simulation. This work may inspire new possibility of constructing high-performance electrode materials through cost-effective strategies but also serve as a fundamental reference for promoting pseudocapacitive energy storage.

Acknowledgements

This work is financially supported by the National Natural Science Foundation of China (Nos. U1662113, 51572296), the Fundamental Research Funds for the Central Universities (15CX08005A), the Financial Support from Taishan Scholar Project (Nos. ts201712020), Technological Leading Scholar of 10000 Talent Project (No. W03020508), Shandong Provincial Natural Science Foundation (ZR2018ZC1458), China and Subsidy of Innovation Project for Postgraduates of China University of Petroleum (YCX2019037).

Appendix A. Supplementary data

Supplementary data to this article can be found online at <https://doi.org/10.1016/j.carbon.2019.07.047>.

References

- [1] P. Simon, Y. Gogotsi, Materials for electrochemical capacitors, *Nat. Mater.* 7 (2008) 845–854.
- [2] B.Y. Guan, X.Y. Yu, H.B. Wu, X.W. Lou, Complex nanostructures from materials based on metal–organic frameworks for electrochemical energy storage and conversion, *Adv. Mater.* 29 (2017) 1703614.
- [3] M.S. Balogun, W.T. Qiu, W. Wang, P.P. Fang, X.H. Lu, Y.X. Tong, Recent advances in metal nitrides as high-performance electrode materials for energy storage devices, *J. Mater. Chem.* 3 (2015) 1364–1387.
- [4] Y.-X. Wang, J. Yang, S.-L. Chou, H.K. Liu, W.-x. Zhang, D. Zhao, S.X. Dou, Uniform yolk-shell iron sulfide–carbon nanospheres for superior sodium–iron sulfide batteries, *Nat. Commun.* 6 (2015) 8689.
- [5] C. Liu, F. Li, L.-P. Ma, H.-M. Cheng, Advanced materials for energy storage, *Adv. Mater.* 22 (2010) E28–E62.
- [6] H.S. Hou, X.Q. Qiu, W.F. Wei, Y. Zhang, X.B. Ji, Carbon anode materials for advanced sodium-ion batteries, *Adv. Energy Mater.* 7 (2017) 1602898.
- [7] N. Nitta, F.X. Wu, J.T. Lee, G. Yushin, Li-ion battery materials: present and future, *Mater. Today* 18 (2015) 252–264.
- [8] Y. Lu, Y. Yu, X.W. Lou, Nanostructured conversion-type Anode materials for advanced lithium-ion batteries, *Chem* 4 (2018) 972–996.
- [9] X. Hu, Y. Li, G. Zeng, J.C. Jia, H.B. Zhan, Z.H. Wen, Three-dimensional network architecture with hybrid nanocarbon composites supporting few-layer MoS₂ for lithium and sodium storage, *ACS Nano* 12 (2018) 1592–1602.
- [10] S. Liu, H. Xu, X. Bian, J. Feng, J. Liu, Y. Yang, C. Yuan, Y. An, R. Fan, L. Ci, Nanoporous red phosphorus on reduced graphene oxide as superior anode for sodium-ion batteries, *ACS Nano* 12 (2018) 7380–7387.
- [11] D. Kong, Y. Wang, Y.V. Lim, S. Huang, J. Zhang, B. Liu, T. Chen, H.Y. Yang, 3D hierarchical defect-rich NiMo₃S₄ nanosheet arrays grown on carbon textiles for high-performance sodium-ion batteries and hydrogen evolution reaction, *Nano Energy* 49 (2018) 460–470.
- [12] Q. Xu, J.-K. Sun, Z.-L. Yu, Y.-X. Yin, S. Xin, S.-H. Yu, Y.-G. Guo, SiO_x encapsulated in graphene bubble film: an ultrastable Li-ion battery anode, *Adv. Mater.* 30 (2018) 1707430.
- [13] J. Han, D. Kong, W. Lv, D.-M. Tang, D. Han, C. Zhang, D. Liu, Z. Xiao, X. Zhang, J. Xiao, X. He, F.-C. Hsia, C. Zhang, Y. Tao, D. Golberg, F. Kang, L. Zhi, Q.-H. Yang, Caging tin oxide in three-dimensional graphene networks for superior volumetric lithium storage, *Nat. Commun.* 9 (2018) 402.
- [14] H. Wang, C. Zhu, D. Chao, Q. Yan, H.J. Fan, Nonaqueous hybrid lithium-ion and sodium-ion capacitors, *Adv. Mater.* 29 (2017) 1702093.
- [15] X. Yao, Y. Ke, W. Ren, X. Wang, F. Xiong, W. Yang, M. Qin, Q. Li, L. Mai, Defect-rich soft carbon porous nanosheets for fast and high-capacity sodium-ion storage, *Adv. Energy Mater.* 9 (2019) 1803260.
- [16] L. Zhou, K. Zhang, Z. Hu, Z. Tao, L. Mai, Y.-M. Kang, S.-L. Chou, J. Chen, Recent developments on and prospects for electrode materials with hierarchical structures for lithium-ion batteries, *Adv. Energy Mater.* 8 (2018) 1701415.
- [17] D. Saurel, B. Orayech, B. Xiao, D. Carriazo, X. Li, T. Rojo, From charge storage mechanism to performance: a roadmap toward high specific energy sodium-ion batteries through carbon anode optimization, *Adv. Energy Mater.* 8 (2018) 1703268.
- [18] C. Zhao, C. Yu, M. Zhang, H. Huang, S. Li, X. Han, Z. Liu, J. Yang, W. Xiao, J. Liang, X. Sun, J. Qiu, Ultrafine MoO₂-carbon microstructures enable ultralong-life power-type sodium ion storage by enhanced pseudocapacitance, *Adv. Energy Mater.* 9 (2017) 1602880.
- [19] L.F. Shen, H.F. Lv, S.Q. Chen, P. Kopold, P.A. van Aken, X.J. Wu, J. Maier, Y. Yu, Peapod-like Li₃VO₄/N-doped carbon nanowires with pseudocapacitive properties as advanced materials for high-energy lithium-ion capacitors, *Adv. Mater.* 29 (2017) 1700142.
- [20] H. He, D. Huang, Y. Tang, Q. Wang, X. Ji, H. Wang, Z. Guo, Tuning nitrogen species in three-dimensional porous carbon via phosphorus doping for ultrafast potassium storage, *Nano Energy* 57 (2019) 728–736.
- [21] Y. Liu, X.-Y. Yu, Y. Fang, X. Zhu, J. Bao, X. Zhou, X.W. Lou, Confining SnS₂ ultrathin nanosheets in hollow carbon nanostructures for efficient capacitive sodium storage, *Joule* 2 (2018) 725–735.
- [22] D.P. Li, X.H. Ren, Q. Ai, Q. Sun, L. Zhu, Y. Liu, Z. Liang, R.Q. Peng, P.C. Si, J. Lou, J.K. Feng, L.J. Ci, Facile fabrication of nitrogen-doped porous carbon as superior anode material for potassium-ion batteries, *Adv. Energy Mater.* 8 (2018) 1802386.
- [23] C.T. Zhao, C. Yu, B. Qiu, S. Zhou, M.D. Zhang, H.W. Huang, B.Q. Wang, J.J. Zhao, X.L. Sun, J.S. Qiu, Ultrahigh rate and long-life sodium-ion batteries enabled by engineered surface and near-surface reactions, *Adv. Mater.* 30 (2018) 1702486.
- [24] Z. Xu, M. Wu, Z. Chen, C. Chen, J. Yang, T. Feng, E. Paek, D. Mitlin, Direct structure-performance comparison of all-carbon potassium and sodium ion capacitors, *Adv. Sci.* (2019) 1802272.
- [25] Z. Xu, J. Liu, C. Chen, H. Potapenko, M. Wu, Hydrophilic binder interface interactions inducing inhesion and capacity collapse in sodium-ion battery, *J. Power Sources* 427 (2019) 62–69.
- [26] C. Chen, M. Wu, Z. Xu, T. Feng, J. Yang, Z. Chen, S. Wang, Y. Wang, Tailored N-doped porous carbon nanocomposites through MOF self-assembling for Li/Na ion batteries, *J. Colloid Interface Sci.* 538 (2019) 267–276.
- [27] L. Wang, T. Sasaki, Titanium oxide nanosheets: graphene analogues with versatile functionalities, *Chem. Rev.* 114 (2014) 9455–9486.
- [28] X.H. Li, S. Kurasch, U. Kaiser, M. Antonietti, Synthesis of monolayer-patched graphene from glucose, *Angew. Chem. Int. Ed.* 51 (2012) 9689–9692.
- [29] J. Liang, X. Du, C. Gibson, X.W. Du, S.Z. Qiao, N-doped graphene natively grown on hierarchical ordered porous carbon for enhanced oxygen reduction, *Adv. Mater.* 25 (2013) 6226–6231.
- [30] S. Wang, X. Yan, K.-H. Wu, X. Chen, J.-M. Feng, P. Lu, H. Feng, H.-M. Cheng, J. Liang, S.X. Dou, A hierarchical porous Fe-N impregnated carbon-graphene hybrid for high-performance oxygen reduction reaction, *Carbon* 144 (2019) 798–804.
- [31] J. Feng, I. Dong, X. Li, D. Li, P. Lu, F. Hou, J. Liang, S.X. Dou, Hierarchically stacked reduced graphene oxide/carbon nanotubes for as high performance anode for sodium-ion batteries, *Electrochim. Acta* 302 (2019) 65–70.
- [32] Y. Fang, Y.Y. Lv, R.C. Che, H.Y. Wu, X.H. Zhang, D. Gu, G.F. Zheng, D.Y. Zhao, Two-dimensional mesoporous carbon nanosheets and their derived graphene nanosheets: synthesis and efficient lithium ion storage, *J. Am. Chem. Soc.* 135 (2013) 1524–1530.
- [33] Y. Wen, K. He, Y. Zhu, F. Han, Y. Xu, I. Matsuda, Y. Ishii, J. Cumings, C. Wang, Expanded graphite as superior anode for sodium-ion batteries, *Nat. Commun.* 5 (2014) 4033.
- [34] J.-S. Wei, C. Ding, P. Zhang, H. Ding, X.-Q. Niu, Y.-Y. Ma, C. Li, Y.-G. Wang, H.-M. Xiong, Robust negative electrode materials derived from carbon dots and porous hydrogels for high-performance hybrid supercapacitors, *Adv. Mater.* 31 (2019) 1806197.
- [35] H. Wang, C. Zhang, Z. Liu, L. Wang, P. Han, H. Xu, K. Zhang, S. Dong, J. Yao, G. Cui, Nitrogen-doped graphene nanosheets with excellent lithium storage properties, *J. Mater. Chem.* 21 (2011) 5430–5434.
- [36] J. Zhang, L. Qu, G. Shi, J. Liu, J. Chen, L. Dai, N,P-Codoped carbon networks as efficient metal-free bifunctional catalysts for oxygen reduction and hydrogen evolution reactions, *Angew. Chem. Int. Ed.* 55 (2016) 2230–2234.
- [37] Q. Lai, Q. Su, Q. Gao, Y. Liang, Y. Wang, Z. Yang, X. Zhang, J. He, H. Tong, In situ self-sacrificed template synthesis of Fe-N/G catalysts for enhanced oxygen reduction, *ACS Appl. Mater. Interfaces* 7 (2015) 18170–18178.
- [38] Y.X. Lu, C.L. Zhao, X.G. Qi, Y.R. Qi, H. Li, X.J. Huang, L.Q. Chen, Y.S. Hu, Pre-oxidation-tuned microstructures of carbon anodes derived from pitch for enhancing Na storage performance, *Adv. Energy Mater.* 8 (2018) 1800108.
- [39] S.H. Choi, G. Nam, S. Chae, D. Kim, N. Kim, W.S. Kim, J. Ma, J. Sung, S.M. Han, M. Ko, H.W. Lee, J. Cho, Robust pitch on silicon nanolayer-embedded graphite for suppressing undesirable volume expansion, *Adv. Energy Mater.* 9 (2019) 1803121.
- [40] C. Ma, C. Deng, X. Liao, Y. He, Z. Ma, H. Xiong, Nitrogen and phosphorus codoped porous carbon framework as anode material for high rate lithium-ion batteries, *ACS Appl. Mater. Interfaces* 10 (2018) 36969–36975.
- [41] J. Yang, X. Zhou, D. Wu, X. Zhao, Z. Zhou, S-doped N-rich carbon nanosheets with expanded interlayer distance as anode materials for sodium-ion batteries, *Adv. Mater.* 29 (2017) 1604108.
- [42] Z. Xiao, Z. Li, P. Li, X. Meng, R. Wang, Ultrafine Ti₃C₂ MXene nanodots-interspersed nanosheet for high-energy-density lithium-sulfur batteries, *ACS Nano* 13 (2019) 3608–3617.
- [43] Y. Liu, L.-Z. Fan, L. Jiao, Graphene highly scattered in porous carbon nanofibers: a binder-free and high-performance anode for sodium-ion batteries, *J. Mater. Chem.* 5 (2017) 1698–1705.

- [44] R. Song, H. Song, J. Zhou, X. Chen, B. Wu, H.Y. Yang, Hierarchical porous carbon nanosheets and their favorable high-rate performance in lithium ion batteries, *J. Mater. Chem.* 22 (2012) 12369–12374.
- [45] P. Li, J. Liu, Y. Wang, Y. Liu, X. Wang, K.-W. Nam, Y.-M. Kang, M. Wu, J. Qiu, Synthesis of ultrathin hollow carbon shell from petroleum asphalt for high-performance anode material in lithium-ion batteries, *Chem. Eng. J. J.* 286 (2016) 632–639.
- [46] Y. Gogotsi, R.M. Penner, Energy storage in nanomaterials – capacitive, pseudocapacitive, or battery-like? *ACS Nano* 12 (2018) 2081–2083.
- [47] P. Xiong, X. Zhang, F. Zhang, D. Yi, J. Zhang, B. Sun, H. Tian, D. Shanmukaraj, T. Rojo, M. Armand, R. Ma, T. Sasaki, G. Wang, Two-dimensional unilamellar cation-deficient metal oxide nanosheet superlattices for high-rate sodium ion energy storage, *ACS Nano* 12 (2018) 12337–12346.
- [48] D. Chao, C. Zhu, P. Yang, X. Xia, J. Liu, J. Wang, X. Fan, S.V. Savilov, J. Lin, H.J. Fan, Z.X. Shen, Array of nanosheets render ultrafast and high-capacity Na-ion storage by tunable pseudocapacitance, *Nat. Commun.* 7 (2016) 12122.
- [49] T. Brezesinski, J. Wang, S.H. Tolbert, B. Dunn, Ordered mesoporous α - MoO_3 with iso-oriented nanocrystalline walls for thin-film pseudocapacitors, *Nat. Mater.* 9 (2010) 146–151.
- [50] Y. Wang, S. Duan, Z. Tian, Y. Shen, M. Xie, X. Guo, X. Guo, Fabrication of TiO_2 @carbon core-shell nanosheets for advanced lithium-ion batteries with excellent cyclability, *J. Mater. Chem.* 5 (2017) 6047–6051.
- [51] S. Niu, Z. Wang, T. Zhou, M. Yu, M. Yu, J. Qiu, A polymetallic metal-organic framework-derived strategy toward synergistically multidoped metal oxide electrodes with ultralong cycle life and high volumetric capacity, *Adv. Funct. Mater.* 27 (2017) 1605332.
- [52] K. Xu, Electrolytes and interphases in Li-ion batteries and beyond, *Chem. Rev.* 114 (2014) 11503–11618.
- [53] C. Zhang, X. Wang, Q. Liang, X. Liu, Q. Weng, J. Liu, Y. Yang, Z. Dai, K. Ding, Y. Bando, J. Tang, D. Golberg, Amorphous phosphorus/nitrogen-doped graphene paper for ultrastable sodium-ion batteries, *Nano Lett.* 16 (2016) 2054–2060.
- [54] N. Zhang, F. Cheng, Y. Liu, Q. Zhao, K. Lei, C. Chen, X. Liu, J. Chen, Cation-deficient spinel ZnMn_2O_4 cathode in $\text{Zn}(\text{CF}_3\text{SO}_3)_2$ electrolyte for rechargeable aqueous Zn-ion battery, *J. Am. Chem. Soc.* 138 (2016) 12894–12901.